Influence of the biomechanical environment on the femoral stem insertion and vibrational behavior: a 3-D finite element study

Anne-Sophie Poudrel, Vu-Hieu Nguyen, Giuseppe Rosi, Guillaume Haiat

Influence of the biomechanical environment on the femoral stem insertion and vibrational behavior: a 3-D finite element study

Anne-Sophie Poudrel[1], Vu-Hieu Nguyen[2], Giuseppe Rosi[2], and Guillaume Haiat*[1]

[1]CNRS, Univ Paris Est Creteil, Univ Gustave Eiffel, UMR 8208, MSME, F-94010 Créteil, France

[2]Univ Paris Est Creteil, Univ Gustave Eiffel, CNRS, UMR 8208, MSME, F-94010 Créteil, France

Abstract

The long-term success of cementless surgery strongly depends on the implant primary stability. The femoral stem initial fixation relies on multiple geometrical and material factors, but their influence on the biomechanical phenomena occurring during the implant insertion is still poorly understood, as they are difficult to quantify *in vivo*. The aim of the present study is

*Corresponding author : guillaume.haiat@univ-paris-est.fr

to evaluate the relationship between the resonance frequencies of the bone-implant-ancillary system and the stability of the femoral stem under various biomechanical environments. The interference fit IF, the trabecular bone Young's modulus E_t and the bone-implant contact friction coefficient μ are varied to investigate their influence on the implant insertion phenomena and on the system vibration behavior. The results exhibit for all the configurations, a non-linear increase of the bone-implant contact throughout femoral stem insertion, until the proximal contact is reached. While the pull-out force increases with E_t, IF and μ, the bone-implant contact ratio decreases, which shows that a compromise on the set of parameters could be found in order to achieve the largest bone-implant contact while maintaining sufficient pull-out force. The modal analysis on the range [2-7] kHz shows that the resonance frequencies of the bone-implant-ancillary system increase with the bone-implant contact ratio and the trabecular bone Young's modulus, with a sensitivity that varies over the modes. Both the pull-out forces and the vibration behavior are consistent with previous experimental studies. This study demonstrates the potential of using vibration methods to guide the surgeons for optimizing implant stability in various patients and surgical configurations.

Keywords femoral stem, finite element analysis, interference fit, bone-implant contact, resonance frequency, primary stability

1 Introduction

Each year, around one million Total Hip Arthroplasties (THA) are performed worldwide, which makes it one of the most common surgeries (Pivec et al. 2012; Sloan et al. 2018). However, surgical failures still occur and up to 10% of revision surgeries are necessary within the ten years after implantation (Ulrich et al. 2008; Corbett et al. 2010), leading to additional costs for the healthcare system and higher pain and risks for the patient (Bayliss et al. 2017). The primary stability of cementless implants is crucial for the surgical success (Khanuja et al. 2011) since aseptic loosening or periprosthetic fractures are among the most frequent causes of failures (Abdel et al. 2016).

Both the Acetabular Cup Implant (ACI) and the Femoral Stem (FS) are inserted into the host bone cavity through successive hammer impacts. The initial fixation is achieved thanks to press-fit phenomena at the bone-implant interface due to an undersized host bone cavity previously reamed by the surgeon (Taylor et al. 1995; Kim et al. 2001). The surgical issue is to maximize the primary stability without increasing the risk of periprosthetic fractures, taking into account the inter-individual variability of bone quality and of the anatomical features. On the one hand, micromotions higher than 150 µm should be avoided, since it has been shown that higher values prevent bone ingrowth (Engh et al. 1992) and therefore osseointegration and implant long-term stability. Moreover, a lack of mechanical loading of the bone tissue because of an imperfect bone-implant interface can cause stress-shielding effects (Raffa et al. 2019a, 2021; Hériveaux et al. 2022), which may lead to the formation of fibrous-tissue (Kuiper and Huiskes 1997) and also inhibit optimal bone ingrowth (Khanuja et al. 2011; Engh et al. 2003; Herrera et al. 2007).

In particular, several studies commonly observed proximal atrophy for the FS due to such phenomena (Engh et al. 1992; Herrera et al. 2007). On the other hand, intra-operative fractures occur around 14 times more often with cementless stems than with cemented (Abdel et al. 2016; Sidler-Maier and Waddell 2015) and lead to revision arthroplasties (Fitzgerald et al. 1988). In particular, due to the nature of the fixation and the shape of the FS implants, the risk of calcar cracks and shaft fractures is significantly increased for cementless implants (Lamb et al. 2019).

The compromise between an optimal fixation and the minimization of fracture risk may be difficult to find for the surgeon as it depends on multiple factors such as: i) the FS design (Folgado et al. 2009; Reimeringer et al. 2013; Monea et al. 2014; Russell et al. 2016; Dopico-González et al. 2010), ii) the patient bone quality (Wong et al. 2005; Shultz et al. 2006), iii) the shape and size of the host bone cavity (Shultz et al. 2006; Abdul-Kadir et al. 2008), iv) the implant coating and porosity (Folgado et al. 2009; Monea et al. 2014; Ovesy et al. 2018) and v) the geometry and mass of the surgical hammer (Bishop et al. 2022). Numerical simulations are therefore valuable to understand the phenomena occurring during implant insertion and in particular to analyze the influence of the biomechanical parameters independently, which is difficult in clinical conditions. While for the ACI, the primary stability may be assessed through the estimation of the pull-out force because of the hemi-spherical shape and the localization of the residual stresses at the ACI rim (Michel et al. 2017; Immel et al. 2021), the Bone-Implant Contact (BIC) ratio and distribution is of particular interest when studying the FS stability, due to the physiological loads and the implant geometry (Monea et al. 2014; Russell et al. 2016; Reimeringer and Nuño 2016). However, according to the studies, the contact ratio achieved after surgery has been reported to vary between 20% and

95% (Monea et al. 2014). Moreover, there is a lack of information concerning the optimal interference fit for the FS (Abdul-Kadir et al. 2008), whereas it has been studied experimentally and numerically for the ACI (Immel et al. 2021; Michel et al. 2017), in order to provide the appropriate range of micromotion and polar gap conducting to successful bone remodeling. Besides, most of the studies on the FS focus on the implant stability during daily activities such as stair climbing or gait loading (Reimeringer et al. 2013; Dopico-González et al. 2010; Abdul-Kadir et al. 2008; Dickinson et al. 2011), that is, when the FS is fully seated. Such approaches give limited insight with respect to the development of intra-operative methods to guide the surgeon in the detection of the optimal insertion end-point, with the ultimate goal to maximize the primary stability and prevent the risk of peri-prosthetic fractures. To reach this long-term objective, the biomechanical phenomena occurring during the FS insertion should be better understood.

Currently, the surgeons detect the insertion end-point by using their proprioception and in particular by listening to the sound of the impact, which is a highly subjective approach. Several experimental studies have explored the use of vibration methods to monitor the FS insertion (Pastrav et al. 2009b; Mulier et al. 2008; Leuridan et al. 2021; Poudrel et al. 2022). A change of the modal features and in particular, a shift of the resonance frequencies, has been evidenced as a function of the implant insertion depth (Poudrel et al. 2022). However, the sensitivity of vibrational analysis with regard to the *BIC* ratio or the bone quality, which is relevant for implant insertion optimization, could not be identified, since it is difficult to measure experimentally. In the literature, the change of the resonance frequency with bone-implant contact conditions has been studied once the implant was fully inserted, either for measuring primary stability (Pastrav et al. 2009a) or

osseointegration (Pérez and Seral-García 2013). Therefore, the change of contact is artificial and these studies do not provide the relation between the frequency change and the implant insertion characteristics.

The present work aims to determine a relationship between the resonance frequencies of the insertion tool, named "ancillary" in what follows, and the implant stability. To do so, a quasi-static 3-D finite element modelling of a FS insertion into a human femur is proposed and a modal analysis is performed at different steps during the insertion. The FS primary stability is evaluated through an estimation of the pull-out force (Shultz et al. 2006; Tijou et al. 2018) and of the bone-implant contact ratio (Monea et al. 2014). The bone stiffness, the bone-implant friction coefficient and the interference fit are varied in order to determine whether the resonance frequency of the bone-implant-ancillary system depends on the FS stability. The originality of the present work is to determine whether a tool capable of measuring the vibrations of the ancillary at different insertion steps could be used in different patients and with different femoral stems to detect the implant insertion end-point.

The paper is organized as follows: after a presentation of the finite element model, the results for the reference case are shown, for both mechanical and vibrational features. Then, the influence of each parameter on the primary stability is studied separately. In addition, the sensitivity of the vibration behavior with regard to the trabecular bone Young's Modulus E_t, and to the bone-implant contact is presented.

2 Material and methods

2.1 Geometry and mesh

The geometrical configuration is described schematically in Fig. 1 where the ancillary, the FS and the femoral bone, cut at its distal end (Pérez and Seral-García 2013; Abdul-Kadir et al. 2008) are shown.

The ancillary was modeled as a cylinder with the same shape and dimensions as in (Poudrel et al. 2022), and bonded to the stem for both the insertion stage and the modal analysis, similarly to the experimental studies (Tijou et al. 2018; Poudrel et al. 2022). The FS geometry was created from the STL file of a scan of the FS RMIS implant of size 9 (CERAFIT RMIS, Ceraver, Roissy, France). The geometry for the human femur was retrieved from a free online database with an appropriate size to accommodate the stem. The cortical layer was created by extrusion using Meshmixer (Autodesk, San Rafael, CA, USA), assuming a constant and uniform thickness of cortical bone tissue of 3 mm, as what was done in (Immel et al. 2021) for an ACI's study. The thickness of the cortical layer was chosen based on experimental measures on bone mimicking phantoms used in (Tijou et al. 2018) and (Poudrel et al. 2022) (ORTHObones, 3B Scientific, Hamburg, Germany), to allow further comparison. The femoral bone cavity was created in ANSYS workbench (v.20, ANSYS Inc., Canonsburg, PA, USA) by boolean subtraction of the rasp volume. The rasp corresponds to the FS, undersized with a scale factor such as the diameter difference between the rasp and the implant, called the interference fit IF, was 200 µm in the reference case. In order to obtain different IF, the FS scale factor was modified. The choice was made to modify the stem geometry rather than the bone cavity, in order to keep the same mesh for the bone.

The mesh was generated in ANSYS Workbench software (v.20, ANSYS Inc., Canonsburg, PA, USA) and consisted in 427,523 tetrahedral elements, which leads to a system of equations with 1,958,289 degrees of freedom. The mesh was finer around the bone implant contact (Fig. 1) and a convergence study on the bone and implant element size h_e and the load step increment Δl_s was conducted for the reference case. Both mesh and load step increment were refined until the implant displacement U_I and BIC ratio, defined by the bone surface in contact with the FS with regard to the total bone cavity surface, local relative errors were less than 5%.

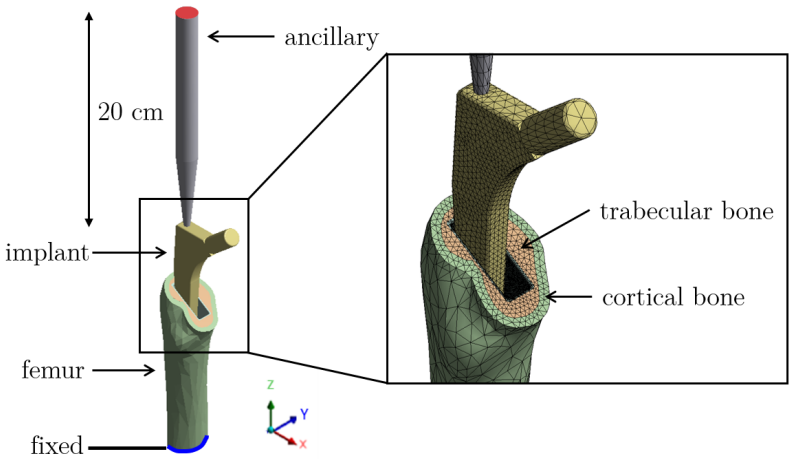

Figure 1: Image of the femur geometry with the FS implant and ancillary and zoom on the mesh close to bone-implant contact. Red elements indicate the region where the load is applied and blue elements indicate the fixed boundary condition.

2.2 Material, interface modeling and parametric study

In order to describe the stem insertion process, the system should be studied under the large displacement assumption. In this context, all materials were assumed to

have isotropic hypoelastic behavior which may be defined by two elastic constants: the Young modulus and the Poisson coefficient. Here, all domains were assumed to be homogeneous and have a same Poisson ratio $\nu = 0.3$. The ancillary and the FS implant were assumed to be made of stainless steel and titanium alloy (Ti-Al6-V4), respectively. The femoral bone was assumed to be composed of trabecular bone surrounded with a 3 mm-thick layer of cortical bone. The Young's moduli of the four domains which constitute the mechanical system are shown in Table 1. A wide range of trabecular bone Young's modulus E_t was investigated, according to physiological values found in the literature (Brown and Ferguson 1980; Bayraktar et al. 2004; Dickinson et al. 2011). The reference value $E_t^* = 0.2$ GPa was chosen according to results on bone mimicking phantoms (Leuridan et al. 2017). As it was previously shown that changes in the trabecular bone modulus have a greater effect on proximal micromotions and strains than cortical properties changes (Wong et al. 2005), the cortical bone Young's modulus E_c was assumed to be fixed and equal to 18 GPa (Katsamanis and Raftopoulos 1990; Bayraktar et al. 2004).

To model different press-fit conditions at the bone-implant interface, interference fit IF values comprised between 100 µm and 400 µm were considered based on results of experimental (Gebert et al. 2009) and numerical studies (Shultz et al. 2006; Abdul-Kadir et al. 2008; Rothstock et al. 2010). The reference value IF^* is not well known in the literature, especially because of the surgeon variability for cavity reaming (Konow et al. 2022) and the specific geometry of the FS. The reference value $IF^* = 200$ µm was chosen with a variation between 100 and 400 µm in order to achieve an acceptable value of bone-implant contact ratio at the end of FS insertion.

Moreover, the frictional contact between the bone and the FS implant was

modeled using Coulomb's law (Wriggers 2006), where

$$f_s = |F_t| - \mu |F_n| \leq 0 \tag{1}$$

$|F_t|$ and $|F_n|$ are the norms of tangential and normal components of interface traction vector, respectively; μ is the friction coefficient; and f_s is a slip criterion which is negative ($f_s < 0$) when no sliding occurs (sticking) and null ($f_s = 0$) in case of sliding. The constant friction coefficient μ was comprised between 0 and 0.5 for the parametric study in order to consider different types of implant coating surfaces and different physiological bone-implant contact conditions (Shirazi-Adl et al. 1993; Dammak et al. 1997; Damm et al. 2015). A reference value of $\mu^* = 0.3$ was chosen (Immel et al. 2021). The bone cavity was decomposed into four distinct regions of interest represented in Fig. 2. The two opposite faces parallel to the frontal plane and the two opposite faces parallel to the sagittal plane constituted the frontal *BIC* (in red in Fig. 2) and the sagittal *BIC* (in blue in Fig. 2), respectively. For solving the contact problem, the Augmented Lagrangian Algorithm, which generally leads to better conditioning and convergence with reasonable number of iteration, was employed (Pettersen et al. 2009; Dopico-González et al. 2010; Reimeringer et al. 2013; Immel et al. 2021).

2.3 Loading, boundary conditions and solver settings

2.3.1 Femoral stem quasi-static insertion

All simulations were carried out under quasi static loading conditions (i.e., excluding inertia and viscosity effects) and taking into account large deformation effects.

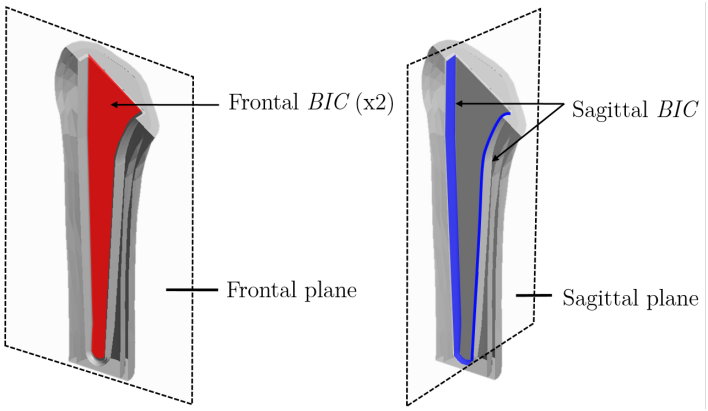

Figure 2: Images of the bone cavity with the *BIC* zones definition regarding the anatomical planes. The frontal and sagittal *BIC* are indicated in red and blue, respectively.

Parameter	Material	Symbol	Density (g/cm^{-3})	Range	Reference value
Ancillary	Stainless steel	-	7.85	-	200 GPa
Implant	TiAl6Al4V	-	4.4	-	113 GPa
Outer bone	Cortical bone	E_c	1.64	-	18 GPa
Inner bone	Trabecular bone	E_t	0.27	[0.1-0.6] GPa	0.2 GPa
Interference fit	-	IF	-	[100-400] µm	200 µm
Friction coefficient	-	μ	-	[0.2-0.5]	0.3

Table 1: Material properties of the four subdomains as well as ranges and reference values of the studied parameters: the trabecular bone Young's modulus E_t (Brown and Ferguson (1980); Bayraktar et al. (2004); Dickinson et al. (2011); Leuridan et al. (2017)), the interference fit IF (Abdul-Kadir et al. (2008); Shultz et al. (2006); Rothstock et al. (2010); Gebert et al. (2009)) and the friction coefficient μ (Shirazi-Adl et al. (1993); Dammak et al. (1997); Damm et al. (2015); Immel et al. (2021)).

A direct solver was used. For all the configurations, the distal region of the femur, which is highlighted in blue in Fig. 1, was assumed to be fixed (Taylor et al. 1995).

The simulation was divided into two stages: i) the implant insertion and ii) the implant pull-out to quantify the primary stability. The imposed vertical load F_z during both the insertion and pull-out stages can be described as a function of

the load step ls by:

$$F_z = \begin{cases} f_0/ls_1 \times ls & \text{for } 0 \leq ls \leq ls_1 \\ -2f_0(ls + ls_1)/(ls_2 - ls_1) + f_0 & \text{for } ls_1 \leq ls \leq ls_2 \end{cases}$$

where ls_1 is defined as the load step when the force F_z starts decreasing and ls_2 corresponds to the last load step of the simulation, when the contact is lost. The load increment between two computations was taken equal to $\Delta ls = f_0/50$ during the implant insertion in order to ensure Newton-Raphson convergence. To simulate the insertion process, a quasi-static vertical load F_z was applied uniformly on the top surface of the ancillary (see Fig. 1) from 0 to $f_0 = 2.5$ kN, corresponding to the load steps $ls = 1$ to $ls_1 = 103$, for all the configurations. The vertical load applied for the simulation of the implant insertion phase will be denoted F_I bellow, in order to distinguish between the insertion and pull-out phases. The value of the imposed force was chosen based on the experiments of (Raffa et al. 2019b) on the ACI. The second stage of the simulation, from $ls_1 = 103$ to $ls_2 = 330$, corresponds to the implant pull-out from the bone which enables to estimate the implant pull-out force F_p.

2.3.2 Bone-stem-ancillary system vibration analysis

At each of ten equally distributed load steps during the FS insertion, pre-stressed modal analysis was performed on the entire bone-implant-ancillary system, similarly at what was experimentally done in (Poudrel et al. 2022). For the modal analysis, the bone-implant interface was assumed to be fully bonded. Only the modes within the frequency range [2-7] kHz were considered in order to allow

comparison with a previous experimental study which demonstrated the sensitivity of several modes regarding implant insertion within this range (Poudrel et al. 2022). Both the resonance frequencies and associated mode shapes were analyzed throughout the implant insertion.

2.4 Femoral stem insertion monitoring and primary stability evaluation

The insertion of the FS implant was monitored by analyzing i) the implant vertical displacement U_I, ii) the BIC ratio variation with respect to the insertion force F_I and iii) the variation of the bone-stem-ancillary system's resonance frequencies with regard to the BIC ratio (Pastrav et al. 2009b; Poudrel et al. 2022).

The FS primary stability was evaluated by i) the value of the pull-out force F_p (Shultz et al. 2006) as what has previously been done for the ACI study (Raffa et al. 2019b; Immel et al. 2021; Doyle et al. 2020) and ii) the BIC ratio at the end of insertion (Monea et al. 2014), that is for $F_I = 2.5$ kN. The pull-out force F_p is defined as the value at the happening of the detachment of the implant from the bone, identified by a slope discontinuity with a brutal decrease of the BIC ratio.

3 Results

3.1 Reference case

3.1.1 Bone-implant contact characteristics during implant insertion

A typical variation of the macroscopic BIC evolution during the implant insertion and pull-out stages is represented in Fig. 3 for the reference case. Four distinct

phases may be identified:

1. contact positioning ($ls \in [0, 60]$, highlighted in grey): at first, $BIC = 0$ as there is no contact between the bone and the implant. As soon as the contact is established ($ls = 28$), the BIC suddenly increases until reaching a "plateau" around 40%. This constant value of the BIC corresponds to a regime in which the non-sliding contact is dominant at the bone-implant interface ($|F_t| < \mu|F_n|$).

2. implant insertion ($ls \in [60, 103]$): this phase corresponds to a regime in which the sliding contact is dominant at the bone-implant interface ($|F_t| = \mu|F_n|$). A detailed description of the BIC evolution during insertion is given in Fig. 4.

3. implant pull-out ($ls \in [103, 308]$): slight decrease of the BIC until a sudden drop to 0% : the slope discontinuity gives the load step corresponding to the pull-out force F_p, (here $ls = 305$).

4. in this last phase, the implant is totally removed from the bone cavity.

Figure 4 studies the macroscopic BIC evolution during FS implant insertion for the reference case, considering the different regions of interest in the cavity presented in Fig. 2. The red and blue curves correspond to the frontal BIC and the sagittal BIC, respectively. Four phases of the BIC can be identified: 1) contact positioning (**A**), 2) frontal BIC increase (**B**), 3) sagittal BIC increase (**C**) and 4) total BIC convergence (**D**). At the end of the FS insertion, that is for $F_I = 2.5$ kN, the BIC reaches 75% of the total bone cavity surface and no further significant contact increase is observed from 2 kN.

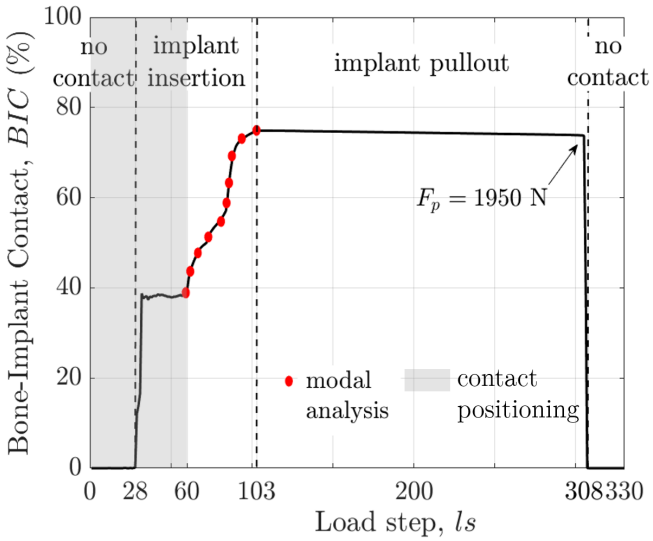

Figure 3: Variation of the BIC ratio as a function of the load step ls during implant insertion and pull-out phases for the reference case E^*, μ^*, IF^*. The red circles indicate the load steps where modal analyses are performed during the insertion phase.

3.1.2 Modal characteristics during femoral stem insertion

The mode shapes and the resonance frequencies in the frequency range [2-7] kHz are represented in Fig. 5 with the same scale factor (0.005) used for the graphical representation of all the deformed shapes. The bone is not shown for a better visualization. Eight modes are represented for which the vibration of the ancillary is of bending nature with two or three nodes. The mode shapes for which the maximum displacement of the ancillary is largely inferior to the maximum displacement of the bone or the femoral stem are not represented since they would not be measurable experimentally.

Figure 6 shows the variation of the resonance frequency of the eight modes as a function of the BIC (Fig. 6a) and the implant relative displacement compared to the bone (Fig. 6b). Only BIC values higher than around 38% are shown since

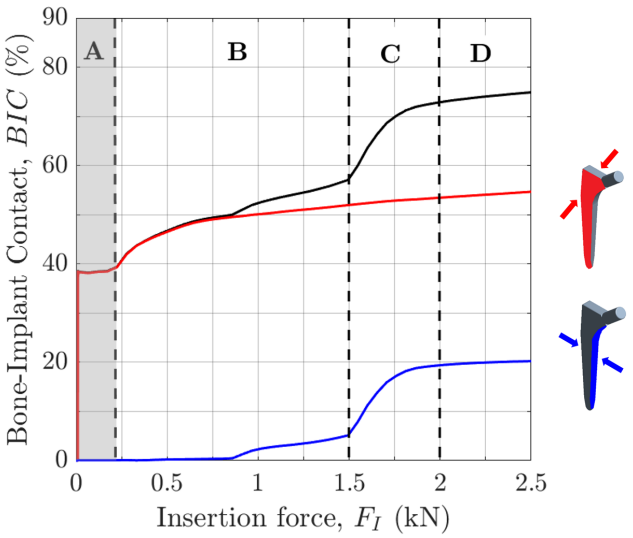

Figure 4: Variation of the BIC ratio considering the full bone cavity (black line), the bone cavity faces parallel to the sagittal plane (blue line) and the bone cavity faces parallel to the frontal plane (red line), as a function of the insertion force F_I for the reference case E^*, μ^*, IF^*.

this level is achieved as soon as the implant is manually positioned in the bone cavity. The three modes f_3, f_4 and f_5 obtained from the simulations correspond to the modes $2Y$, $2X$ and $2Y_b$ measured experimentally in (Poudrel et al. 2022) in terms of bending shapes and of values of the resonance frequency. The resonance frequencies of the modes $2Y$ and $2Y_b$ increase until reaching a value close to 3.8 kHz and 4.5 kHz, respectively, which is consistent with our experimental study. Moreover the mode $2X$ shows a smaller resonance frequency variation, especially for $BIC > 55\%$, which is in good agreement with what was obtained experimentally in (Poudrel et al. 2022). Therefore, in what follows, only these three modes will be selected for the study on the sensitivity to the trabecular bone Young's modulus E_t.

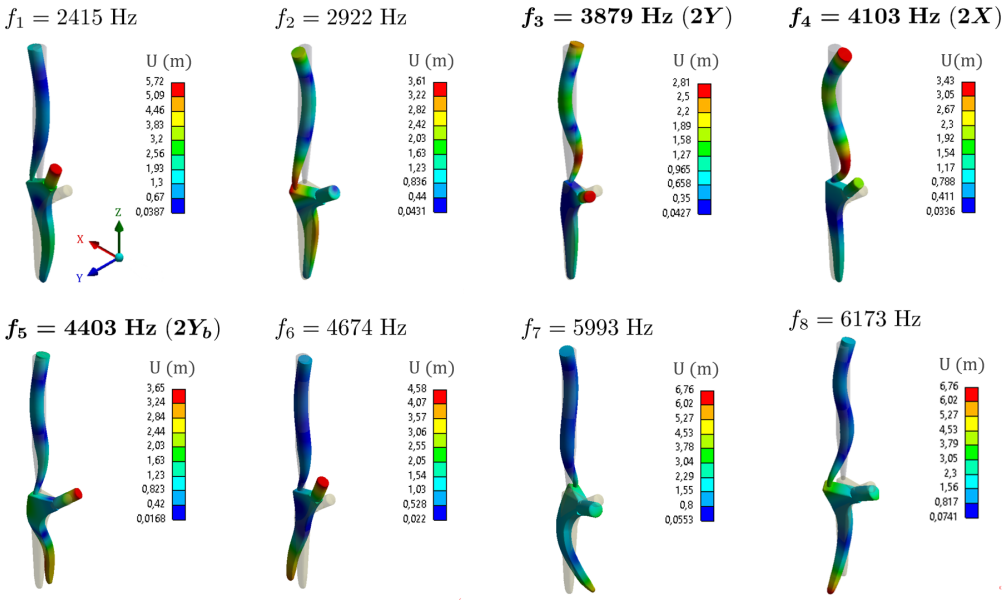

Figure 5: Mode shapes and corresponding resonance frequencies in the range [2-7] kHz obtained at the end of the FS insertion ($F_I = 2.5$ kHz), for the reference case E^*, μ^*, IF^*. The modes $2Y$, $2X$ and $2Y_b$, highlighted in bold, corresponds to the experimental modes identified in (Poudrel et al. 2022).

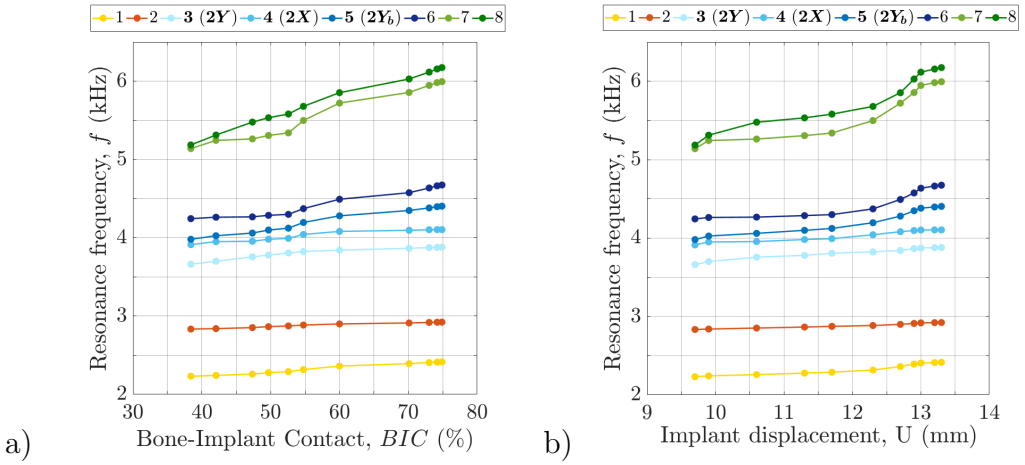

Figure 6: Variation of the bone-implant-ancillary system resonance frequencies f in the range [2-7] kHz as a function of (a) the BIC ratio and (b) the implant displacement U_I. The modes $2Y$, $2X$ and $2Y_b$ are highlighted in bold and correspond to the experimental modes identified in (Poudrel et al. 2022).

3.2 Implant insertion monitoring under different biomechanical parameters

3.2.1 Effect of trabecular bone Young's modulus

Figure 7 shows the influence of the trabecular bone Young's modulus E_t on the variation of the implant displacement U_I and on the BIC as a function of the insertion force F_I. Both the implant displacement U_I and the BIC increase when E_t decreases. For the three smallest values of E_t ($E_t = 0.1$ GPa, $E_t^* = 0.2$ GPa and $E_t = 0.3$ GPa), the curves corresponding to the variation of the implant displacement U_I as a function of F_I exhibit a slope discontinuity, which corresponds to the jump of the BIC evolution explained by the establishment of the sagittal BIC (see Fig. 4 and Fig. 7b). The value of F_I where this discontinuity occurs increases as a function of the Young's modulus E_t. At the end of the insertion stage ($F_I = 2.5$ kN), the BIC varies from 50% to 82% depending on the value of the trabecular bone Young's modulus, which corresponds to a difference of implant displacement U_I close to 2.5 mm.

3.2.2 Effect of friction coefficient

Figure 8 shows the influence of the friction coefficient μ on the variation of the implant displacement U_I (a) and the BIC (b) as a function of the insertion force F_I. The implant displacement U_I and the BIC are higher for smaller values of the friction coefficient μ. Except for the highest value of the friction coefficient ($\mu = 0.5$), the curves corresponding to the variation of the implant displacement U_I as a function of F_I exhibit a slope discontinuity, which corresponds to the jump of the BIC evolution explained by the establishment of the sagittal BIC (see Fig.

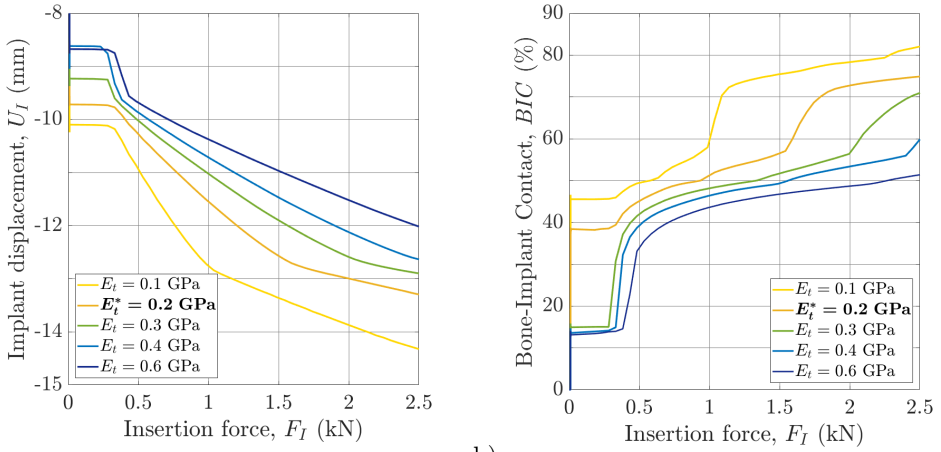

Figure 7: Variation of (a) the implant displacement U_I and (b) the BIC ratio as a function of the insertion force F_I for different values of the trabecular bone Young's modulus E_t. The reference case E_t^* is highlighted in bold.

4 and Fig. 8b). At the end of insertion ($F_I = 2.5$ kN), the difference of implant displacement U_I reaches 1 mm for friction coefficient μ comprised in the range [0.2-0.5]. It is worth noting that this small difference in the displacement, difficult to measure in the clinic, corresponds to a variation of BIC of nearly 20%.

3.2.3 Effect of interference fit

Figure 9 shows the influence of the interference fit IF on the variation of the implant displacement U_I (a) and the BIC (b) as a function of the insertion force F_I. The values of implant displacement U_I and of the BIC for any insertion force F_I decrease as a function of the interference fit IF. For the three smallest values of IF ($IF = 100$ µm, $IF = 150$ µm, $IF = 200$ µm), the curves corresponding to the variation of the implant displacement U_I as a function of F_I exhibit a slope discontinuity, which corresponds to the jump of the BIC evolution explained by the establishment of the sagittal BIC (see Fig. 4 and Fig. 8b). For values of IF

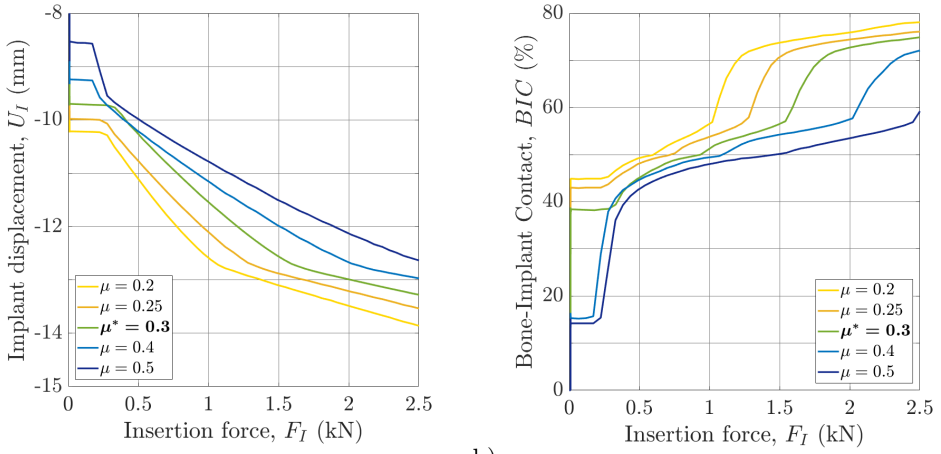

Figure 8: Variation of the implant displacement U_I (a) and the BIC ratio (b) as a function of the insertion force F_I for different values of the friction coefficient μ. The reference case μ^* is highlighted in bold.

between 100 µm and 400 µm, the values of the implant displacements U_I at the end of the insertion ($F_I = 2.5$ kN) are equal to 15 mm and 9 mm, respectively, while the corresponding BIC ratio varies from 80% to 60%. Increasing the value of the interference fit leads to lower implant displacement U_I and lower BIC value reached at the end of the insertion, which may be explained by an increase of the normal forces due to contact pressure. For the range of variations considered in the present study for μ and IF, the effect of the interference fit on the implant displacement is lower than that of the friction coefficient.

3.3 Variation of the FS implant stability

Figure 10 shows the variation of the pull-out force F_p and of the BIC ratio at the end of insertion stage ($F_I = 2.5$ kN) as a function of (a) the trabecular bone Young's modulus E_t, (b) the friction coefficient μ and (c) the interference fit IF. For each parametric study, the results are given with all other parameters fixed at

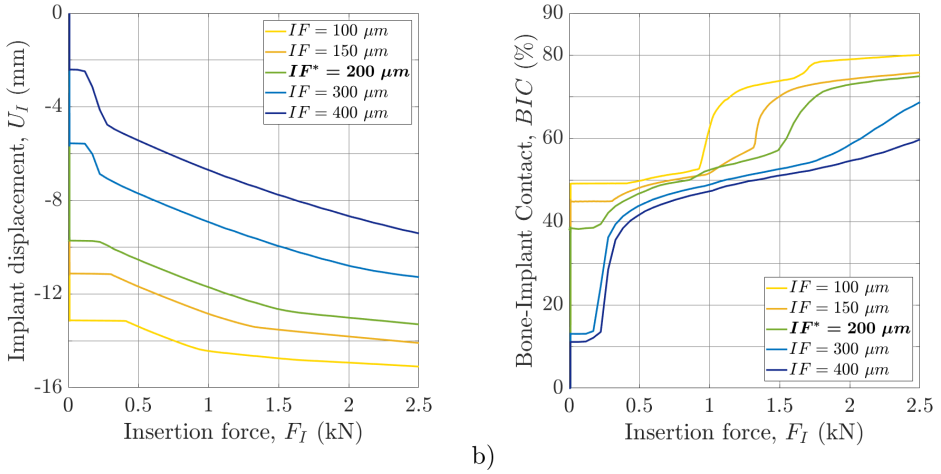

Figure 9: Variation of the implant displacement U_I (a) and the BIC ratio (b) as a function of the insertion force F_I for different values of the interference fit IF. The reference case IF^* is highlighted in bold.

the reference value, noted by *. Figure 10 shows an increase of the pull-out force with the parameters E_t, μ or IF. Conversely, the BIC ratio decreases as a function of E_t, μ, IF. The pull-out force F_p has a strong non-linear behavior as a function of IF, with a strong increase for IF values between 100 µm and 150 µm and a significantly lower increase for $IF > 150$ µm. A good compromise is obtained for the reference case with the maximization of both the BIC and the pull-out force F_p reaching 75% and 1.95 kN, respectively. The values of the pull-out force F_p found in Fig. 10 are again in good agreement with experimental results obtained on bone mimicking phantoms (Tijou et al. 2018). An optimal range of values can be defined for μ, and IF (an optimal value of E_t is not searched here as it is not a parameter controllable by the surgeon), which optimize the FS stability by maximizing both the pull-out force F_p and the BIC ratio. For instance, friction coefficient values between 0.25 and 0.35 and IF values between 150 µm and 250 µm provide FS stability such as $F_p > 1.9$ kN and $BIC > 70\%$.

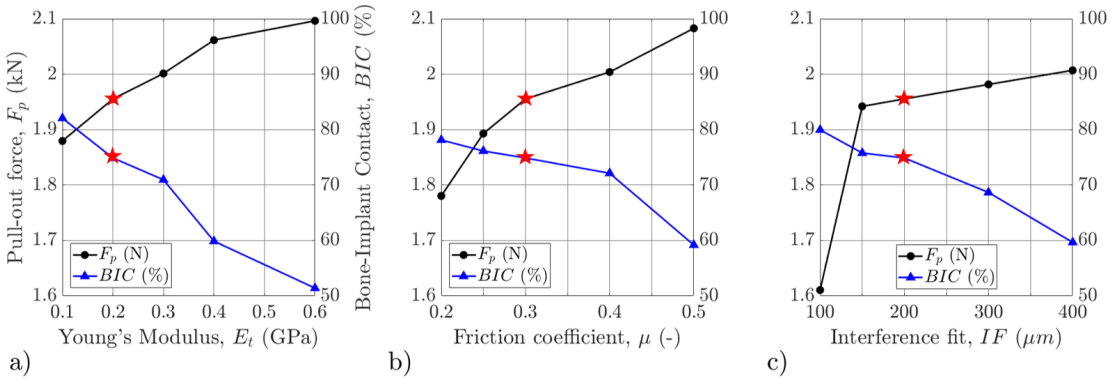

Figure 10: Variation of the pull-out force F_p and the BIC ratio measured at the end of the FS insertion ($F_I = 2.5$ kN) as a function of the trabecular bone Young's modulus E_t (a), the friction coefficient μ (b) and the interference fit IF (c). The red stars indicate the values obtained for the reference case E_t^*, μ^* and IF^*.

3.4 FS insertion monitoring by means of modal analysis

Figures 11, 12 and 13 show the variation of the resonance frequencies of modes $2Y$ (a), $2X$ (b) and $2Y_b$ (c) as a function of the BIC ratio evolution during implant insertion for different values of trabecular bone Young's modulus E_t, friction coefficient μ and interference fit IF, respectively. Each marker is the result of the modal analysis performed during implant insertion, noted by red circles in Fig. 3. For all values of the bone stiffness, of the friction coefficient and of the interference fit, the resonance frequencies of the modes $2Y$ and $2Y_b$ increase with the BIC ratio in the ranges considered herein. The mode $2X$ appears to be less sensitive than the two others modes to the implant insertion. Moreover, for a constant value of the BIC ratio, while the bone stiffness influences the resonance frequencies (see Fig. 11), they do not depend on the friction coefficient (see Fig. 12) and on the interference fit (see Fig. 13). In particular, for a given BIC ratio, the value of the resonance frequencies of mode $2Y$ and $2Y_b$ increases when the bone stiffness increases (see Fig. 11). The mode $2X$ does not seem to be influenced by trabecular bone Young's

modulus E_t higher than 0.3 GPa. These results are consistent with the boundary conditions considered between the bone and the implant during the modal analyses since the friction coefficient only influences the insertion phenomena (implant displacement and BIC ratio, see Fig. 8) and not the modal analysis during which the bone-implant interface is considered to be linear and fully bounded. Therefore, considering the same level of BIC ratio, which correspond to similar implant positions, the system resonance frequencies are not significantly different.

More specifically, an approximately linear relation between the resonance frequency and the BIC ratio is obtained for each mode and each value of E_t. The sensitivity of each mode to the BIC may be assessed by the slope of the linear regression curve for each value of E_t, which is indicated in Table 2 together with the corresponding correlation coefficient R^2. Considering the reference case, the most sensitive mode is the mode $2Y_b$, with a mean sensitivity of 14.03 Hz/%. This sensitivity is similar for the different values of E_t within the range [0.1 0.6] GPa. The least sensitive mode is $2X$, with a slope inferior to 2 Hz/% for $E_t = 0.3$ GPa, $E_t = 0.4$ GPa and $E_t = 0.6$ GPa. However, the sensitivity of $2X$ is higher for the smallest trabecular bone Young's modulus, reaching up to 12.95 Hz/% for $E_t = 0.1$ GPa, which may be explained by large differences of implant position for the same level of BIC ratio. In addition, the sensitivity of the resonance frequency to the trabecular bone Young's modulus E_t is evaluated at a given BIC ratio, indicated by the vertical dashed line at $BIC = 50\%$ in Fig. 11. The resonance frequency of each mode obtained at $BIC = 50\%$ is noted $f_{BIC=50\%}$ and the values are shown in Table 2 for the different values of E_t. The mode $2Y_b$ is the most sensitive to the trabecular bone Young's modulus E_t, with a variation of more than 1.1 kHz obtained for values of E_t varying between 0.1 GPa and 0.6 GPa. The modes $2Y$

and $2X$ are more sensitive to changes of the trabecular bone Young's modulus when small values of E_t are considered. In particular, the resonance frequency of the mode $2X$ is nearly constant for $E_t > 0.3$ GPa, with a frequency variation lower than 30 Hz between $E_t = 0.3$ GPa and $E_t = 0.6$ GPa.

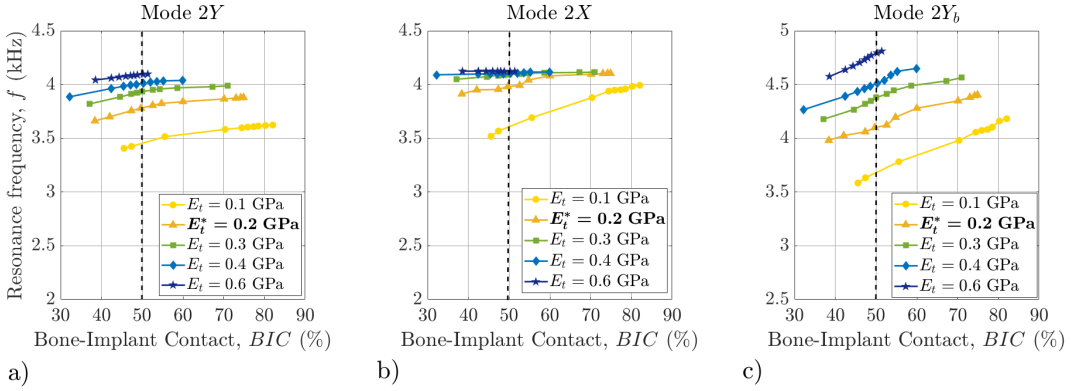

Figure 11: Variation of the bone-stem-ancillary system resonance frequencies f corresponding to the mode $2Y$ (a), the mode $2X$ (b) and the mode $2Y_b$ (c) as a function of the BIC ratio for different values of the trabecular bone Young's modulus E_t. The vertical dashed line at $BIC = 50\%$ is used to determine the sensitivity of f to E_t for a constant value of the BIC ratio by assessing $f_{BIC=50\%}$, which corresponds to the value of f for $BIC = 50\%$ (see Table 2).

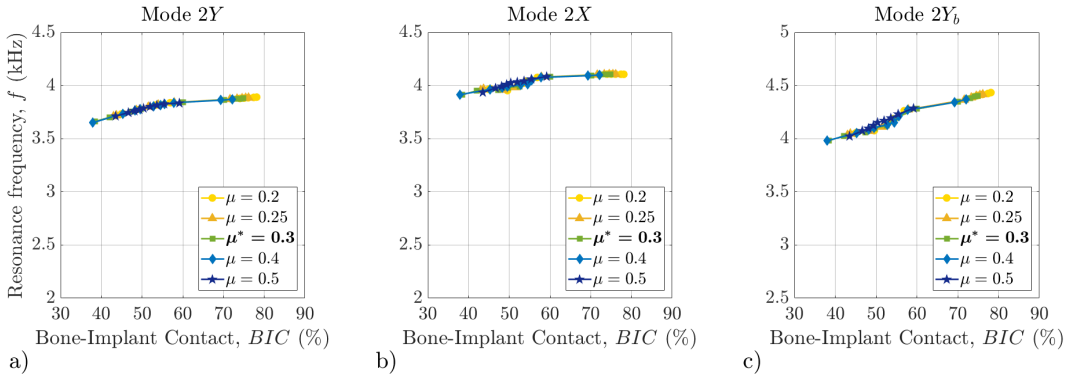

Figure 12: Variation of the bone-stem-ancillary system resonance frequencies f corresponding to the mode $2Y$ (a), the mode $2X$ (b) and the mode $2Y_b$ (c) as a function of the BIC ratio for different values of the friction coefficient μ.

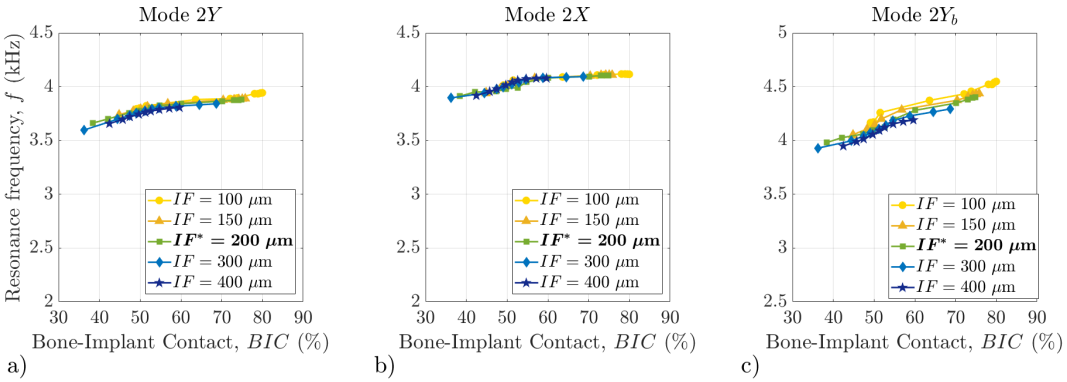

Figure 13: Variation of the bone-stem-ancillary system resonance frequencies f corresponding to the mode $2Y$ (a), the mode $2X$ (b) and the mode $2Y_b$ (c) as a function of the BIC ratio for different values of the interference fit IF.

E_t (GPa)		0.1	0.2	0.3	0.4	0.6	Mean	Std
slope (Hz/%)	$2Y$	5.81	5.28	4.53	5.75	4.34	5.14	0.68
	$2X$	12.95	5.26	1.80	1.04	-0.17	4.13	5.30
	$2Y_b$	12.95	11.86	11.47	14.82	19.07	14.03	3.10
R^2	$2Y$	0.97	0.90	0.83	0.95	0.99	0.93	0.06
	$2X$	0.99	0.93	0.85	0.87	0.57	0.84	0.16
	$2Y_b$	0.99	0.98	0.95	0.98	0.99	0.98	0.02
$f_{BIC=50\%}$ (Hz)	$2Y$	3453.6	3781.9	3933.3	4018.8	4093.5	3856.2	253.1
	$2X$	3680.5	3982.4	4093.5	4101.7	4123.0	3996.2	184.8
	$2Y_b$	3607.2	4101.3	4377.4	4507.2	4790.1	4276.6	448.8

Table 2: Slope and determination coefficient (R^2) corresponding to the linear regression analysis of the variation of the resonance frequency as a function of the BIC ratio for the modes $2Y$, $2X$ and $2Y_b$. Values of the resonance frequency of the modes $2Y$, $2X$ and $2Y_b$ evaluated at $BIC = 50$ % for different trabecular bone Young's modulus E_t (see dashed lines in Fig. 11).

4 Discussion

This work aims to provide more insight into the influence of various biomechanical parameters on the FS insertion and primary stability, which could lead to eventually develop a vibration-based method to guide surgeons during the insertion procedure. The contact ratio and the pull-out force depend on the trabecular bone Young's modulus E_t, the friction coefficient μ and the interference fit IF. The

resonance frequencies of the bone-implant-ancillary are shown to be sensitive to the bone-implant contact BIC ratio and to the trabecular bone Young's modulus E_t. The corresponding mode shapes and the variation of the resonance frequencies during the FS insertion are in good agreement with experimental measurements performed in a previous work by our group (Poudrel et al. 2022).

4.1 Bone-implant contact evolution

During the FS insertion, the BIC evolution is found to increase non-linearly with the insertion force for all configurations, which is in good agreement with the dynamic finite element study of (Monea et al. 2014) on the evolution and distribution of the bone-implant contact during and after the FS insertion. This non-linear increase of the BIC ratio may be explained by the particular shape of the FS implant : the BIC at the sagittal bone cavity faces is established after the BIC at the frontal bone cavity faces (see Fig. 4). In particular, the contact reached in the calcar zone, which is part of the sagittal BIC is of great interest for the surgeons because this femur region is subjected to periprosthetic fractures (Abdel et al. 2016) and stress-shielding effects (McCarthy et al. 1991; Joshi et al. 2000; Khanuja et al. 2011). The contact evolution obtained for the reference case indicates that continuing the stem insertion into the cavity for insertion forces F_I higher than 2 kN does not lead to a significant increase in BIC ratio (see Fig. 4). This observation validates the choice of $IF^* = 200$ µm as a reference value and confirms the need for the surgeons to detect the insertion end-point in order to avoid stress concentration which could lead to periprosthetic bone fractures (Kim et al. 2001) and to surgical failure.

4.2 Femoral stem pull-out

The simulated pull-out forces are comprised between 1611 N and 2096 N, which is in good agreement with experimental values obtained on bone mimicking phantoms in (Tijou et al. 2018), where the pull-out forces were found to be between 1000 and 2300 N according to the stability configuration. The pull-out force is found to be an increasing function with respect of the bone's stiffness, the friction coefficient and the interference fit. It is worth noting that these results are new findings, because in the literature, the other studies on FS's biomechanical behavior rather focused on the micromotion than the pull-out force evaluation. The fact that the pull-out force of the femoral stem increases as a function of various parameters (interference fit, bone stiffness, friction) may be helpful to improve the implant design (friction coefficient) and the insertion procedure (interference fit) in order to maximize the implant stability. Moreover, to maximize the FS primary stability, the BIC ratio should also be considered in addition to the pull-out force, as discussed in Section 4.3.

In previous studies on the ACI, it was shown that the pull-out force increases with these same parameters until an optimal value and then decreases for higher values (Raffa et al. 2019b; Immel et al. 2021). This behavior may be explained by the fact that highly concentrated contact stresses appearing at the equatorial rim of ACI strongly increase with the increasing variation of (E_t, μ, IF), which may prevent the implant to be completely inserted into the bone cavity under the physiological driving force, leading to a worse pull-out force. However, in the case of FS considered herein, as the bone-implant contact surface is much larger, the contact force is not sufficiently strong, even for the biggest values of (E_t, μ, IF),

to prevent the complete insertion of the implant into the bone cavity under the considered imposed force. Consequently, the pull-out force of FS was found to monotonously increase with the aforementioned parameters. A simplified cone-shape implant model from (Shultz et al. 2006) confirms our finding concerning the pull-out force, which is found to increase with the interference fit or the friction coefficient, with values between 8000 N and 9000 N. The higher pull-out forces F_p observed in (Shultz et al. 2006) than in Fig. 10 may be due to the use of cortical bone only, which has a Young's modulus 100 times higher than the trabecular bone material used in the present finite element model. This interpretation is coherent with the increase of the pull-out force with the trabecular bone Young's modulus E_t shown in Fig. 10a.

4.3 Optimal configurations for maximizing FS primary stability

While the polar gap and the pull-out force are key determinants of the ACI stability (Immel et al. 2021; Raffa et al. 2019b; Doyle et al. 2020), the FS insertion success mainly depends on the *BIC* ratio and the stress distribution in the host bone (Kim et al. 2001; Monea et al. 2014; Russell et al. 2016; Reimeringer and Nuño 2016). Due to the anatomical distribution of muscular and joint loads, optimizing the FS pull-out force in the case of the FS is less crucial for the surgical success than minimizing micromotion at the bone-implant interface, which influence the osseointegration and the bone remodelling phenomena (Engh et al. 1992; Herrera et al. 2007; Folgado et al. 2009). Therefore, the effect of the bone quality, of the friction coefficient at the bone-implant interface and of the stem geometry

has been widely studied in the literature for the optimization of the long-term stability evaluated from the micromotion retrieved during daily activities such as stair climbing or walking (Dopico-González et al. 2010; Dickinson et al. 2011; Reimeringer et al. 2013; Russell et al. 2016). However, the pull-out force remains useful to evaluate quantitatively the primary stability (Tijou et al. 2018) in order to identify factors influencing the immediate fixation strength as bone property (Shultz et al. 2006) or implant design.

Concerning the effect of bone quality, it has been shown in the literature that both the reduction of the elastic modulus of cortical and trabecular bone caused an increase of the initial micromotion and the bone strain at the bone-implant interface (Wong et al. 2005). As shown in Fig. 10a, the initial fixation strength decreases when E_t decreases, which may be explained by lower interface stresses even if the global bone-implant contact is higher. This result proves the importance to not only consider the pull-out force but also the level of the *BIC* ratio when studying FS stability. This same results also emphasizes the necessity to consider the bone quality parameter when comparing with experimental results. Concerning the influence of the friction coefficient, it was found in the literature that higher levels of coefficient of friction are beneficial to primary fixation (Shultz et al. 2006), which is in good agreement with our results presented in Fig. 10b where the pull-out force increases from 1780 N to 2090 N when the friction coefficient increases from $\mu = 0.2$ to $\mu = 0.5$. However, a friction coefficient of $\mu = 0.5$ should be avoided since the *BIC* ratio at the end of FS insertion is not converged (see Fig. 8b), indicating that the maximum contact level at the sagittal faces and in particular in the calcar zone is not achieved.

While the studies on the ACI confirm the existence of an optimal interference

fit for maximizing primary stability (Immel et al. 2021), the existence of such optimal configuration is less obvious for the FS. Due to the geometry of the FS, the effective value of the interference fit resulting from the cavity reaming is difficult to control, which leads to a huge variability on the cavity preparation between surgeons (Konow et al. 2022). Several studies on FS micromotion optimization fond significantly lower optimal interference fit values than for the ACI (Abdul-Kadir et al. 2008; Pettersen et al. 2009; Russell et al. 2016). The results found herein indicate that an interference fit under 150 µm significantly decreases the pull-out force without providing a significantly higher bone-implant contact ratio (see Fig. 10c). The behavior of the pull-out force with regard to the interference fit is in good agreement with a similar study considering both elastic and viscoelastic bone properties and a simplified cylindrical stem, where an interference fit "threshold" was evidenced beyond which no additional gains in push-out load are achieved (Shultz et al. 2006). However, other studies in the literature predict smaller optimal interference fit levels, around 50 µm, to achieve good primary stability fixation while avoiding femoral canal fracture (Abdul-Kadir et al. 2008; Pettersen et al. 2009). In clinic, these levels of interference fit are difficult to reach with manual reaming and experimental results show that the interference fit corresponding to such micromotion obtained from FE analysis are more likely to be of 1-2 µm (Abdul-Kadir et al. 2008).

4.4 Modal analysis: a tool to monitor FS insertion

The resonance frequencies of the bone-stem-ancillary system and their evolution with the implant insertion into the bone are found to be in good agreement with

previous experimental results obtained with a bone mimicking phantom (Poudrel et al. 2022). In this previous study (Poudrel et al. 2022), two bending modes vibrating in a plane parallel to the sagittal one, namely the modes *2Y* and $2Y_b$, with a mean frequency of 2875 Hz and 3496 Hz over the specimens, were found to be sensitive to the implant insertion depth into the bone cavity. Another mode shape named *2X* and oscillating parallel to the frontal plane was also measured. Its resonance frequency was around 3129 Hz and did not change significantly during implant insertion. The number of modes obtained numerically is found to be higher than experimentally (see Fig. 5), which can be explained by the experimental method employed to retrieve the mode shapes, based on the measure of accelerations all along the ancillary axis, which were recorded consecutively to an excitation by an hammer impact. Therefore, only the modes with the most important ancillary vibration amplitude were recorded in the previous study (Poudrel et al. 2022).

For the reference case ($E_t^* = 0.2$ GPa, $\mu^* = 0.3$, $IF^* = 200$ µm), the numerical results corresponding to modes *2Y*, $2Y_b$ and *2X* (highlighted in bold in Fig. 5) were identified based on their mode shape and resonance frequency, which are both coherent with experimental data, even if the frequencies are slightly higher. However, the boundary conditions, the bone material properties, the implant coating and friction coefficient, and the effective experimental interference fit may be slightly different in the numerical and experimental studies, which may explain such difference. However, the variation of the resonance frequencies with the implant displacement (see Fig. 6b) is in good agreement with experimental data (Poudrel et al. 2022). In particular, the numerical model confirms the sensitivity of the modes $2Y$ and $2Y_b$ to the *BIC* ratio (see Fig. 6a), which could not have

been measured in the experimental study (Poudrel et al. 2022). Moreover, the resonance frequency of the mode $2X$ is found not to increase for $BIC > 55\%$, which is a value likely to be reached during the first steps of implant insertion and corroborates the non-sensitivity of the mode $2X$ observed experimentally (Poudrel et al. 2022). Table 2 shows that the most sensitive mode for insertion monitoring is $2Y_b$ with a variation of 14 Hz per $\%BIC$ increase. Such a frequency increase during implant insertion could be easily measured experimentally since the frequency resolution of the experimental device developed in Poudrel et al. (2022) is 4 Hz. In addition, a lower increase of the eight resonance frequencies in the range [2-7] kHz is observed at the end of FS insertion than at the beginning, and in particular for $U_I > 13$ mm (see Fig 6b), which is explained by the fact that the increase of BIC ratio is lower at the end of the insertion (see Fig. 4). Experimentally, the modes $2Y$ and $2Y_b$ increased as a function of the insertion step, until they reached a threshold and stayed constant (Poudrel et al. 2022). The insertion step corresponding to the convergence was in good agreement with the convergence of the implant displacement and with the results obtained by another implant insertion monitoring method based on the impact force analysis (Poudrel et al. 2022). This result confirms that such a frequency convergence may be of interest to detect insertion end-point, which corresponds to the moment when continuing to push the implant into the bone will not lead to any better implant fixation or higher BIC increase.

Different numerical studies considered the resonance frequency shift with contact conditions in order to simulate osseointegration and therefore investigate the mode sensitivity to the long-term stability (Pastrav et al. 2009a; Pérez and Seral-García 2013). Similarly as in our study, the resonance frequency shift with the

583 bone-implant contact was shown to depend on the mode number and on the loca-
584 tion of the BIC : proximal, distal or central (Pastrav et al. 2009a). The highest
585 frequency shifts were observed for proximal contact increase. In the perspective
586 of the development of a surgical tool, being able to estimate the amount of bone-
587 implant contact thanks to the measure of the bone-implant-ancillary system reso-
588 nance frequencies is of great interest. In particular, it can prevent periprosthetic
589 bone fractures by avoiding non-necessary hammer impacts if the BIC ratio has
590 already converged (Fig. 4). The results shown in Fig. 6 highlight that two modes
591 are particularly sensitive to the bone-implant contact ratio, namely the modes 7
592 and 8, which were not identified in the previous experimental study (Poudrel et al.
593 2022). An optimization of the sensor positioning on the ancillary, according to the
594 mode shape, could be relevant to be able to measure these modes experimentally.

595 The sensitivity of the resonance frequency to E_t is found to depend on the
596 mode of vibration (see Fig. 11). For the same level of BIC, while the frequencies
597 of the modes $2Y$ and $2Y_b$ increase with the trabecular bone Young's modulus
598 (Fig. 11a and 11c), the frequency of the mode $2X$ is constant for high bone
599 rigidity ($E_t > 0.2$ GPa) (Fig. 11b). This variation of sensitivity depending on
600 the mode number was also observed in a study focusing on the stem material
601 properties (Pérez and Seral-García 2013), where the frequency shift observed for
602 various implant materials varied according to the mode number. A global increase
603 of the resonance frequencies is observed for stiffer materials considering the same
604 level of bone-implant contact, which is in good agreement with our findings. This
605 observation may be of interest for the surgeons in order to retrieve information on
606 the patient bone quality or to adapt the surgical protocol. Moreover, as shown in
607 Fig. 12 and 13, the resonance frequencies of mode $2Y$, $2X$ and $2Y_b$ do not depend

on the friction coefficient and the interference fit, respectively, while they increase as a function of the *BIC* ratio. This behavior is explained by the sensitivity of the resonance frequencies to the bone-implant system stiffness, which depends on the quantity of bone-implant contact. Although the friction coefficient and the interference fit influences the implant insertion (and in particular the implant displacement and bone-implant contact, see Fig. 8), the values of *IF* and μ do not affect the measurement of the resonance frequencies for a given *BIC* value, as the bone-implant interface was assumed to be fully bonded and linear for the modal analysis. As a conclusion, this analysis confirms that the vibration method studied herein, and in particular the monitoring of the resonance frequencies, may lead to an estimation of the *BIC* ratio, provided that bone quality is known, which is currently difficult to measure by the surgeon.

4.5 Limitations of the FE model

This study has several limitations. First, only a single type of FS and ancillary geometry was studied due to the numerous parameters considered and to computation time related issues. However, the FS design considered in this work -straight stem with a cervico diphyseal angle of 132°, a medial curvature adapted to different morphologies to avoid post-operative varus (uncemented femoral stem)- is largely employed by the surgeons for uncemented procedures. Therefore, the results obtained herein are of interest for a majority of uncemented procedures. However, the influence of other shapes of implant could be considered in a future work, based on studies about the effect of the implant geometry on the level of stress and micromotion under cyclic loading (Dopico-González et al. 2010; Reimeringer

et al. 2013; Russell et al. 2016) or on the bone remodeling (Folgado et al. 2009). Several recent reports also provide insight on the contribution of FS design to the risk of periprosthetic fractures (Khanuja et al. 2011; Carli et al. 2017). A change of femur geometry should also be considered in order to represent the patient variation (Pettersen et al. 2009). Eventually, although considering half of the femur with the fixation of the distal end is commonly employed when studying femoral stem insertion (Taylor et al. 1995; Pérez and Seral-García 2013; Abdul-Kadir et al. 2008; Tijou et al. 2018; Poudrel et al. 2022), such configuration is likely to affect the values of the bone-implant-ancillary system resonance frequencies, compared to a real anatomic configuration. Since the resonance frequencies depend on the system rigidity, the length of the femur as well as the boundary condition at the distal part may affect their quantitative values. However, the vibration behavior with regard to the implant insertion should not be affected since these geometrical and boundary conditions do not vary throughout the implant insertion procedure. In addition, the same geometry of the femur as well as the same distal boundary condition were used for the parametric study, which allows to compare the results across the configurations. Note that in the context of acetabular cup insertion, we showed that adding soft tissue around the bone receiving the implant does not significantly modify the results obtained using the instrumented hammer (Tijou et al. 2018; Bosc et al. 2018). Eventually, the configuration of the numerical model represents the experimental one of Poudrel et al. (2022) and the results obtained using the two approaches could be compared. Although the results cannot be directly translated to the clinical practice, the model may help to understand the vibration behavior of the bone-implant-ancillary system during the implant insertion procedure.

Second, we assumed that bone is homogeneous, elastic and isotropic. However, the bone properties are inhomogenous, as shown by several authors who used CT scans to recover the spatial distribution of the bone density (Ovesy et al. 2018). Even if the same computational procedure could have been followed, the aim was to determine the effect of the global bone stiffness on the FS insertion. The effect of bone anisotropic properties have been investigated for the ACI stability (Nguyen et al. 2017), but was not used in the present study herein in order to simplify the configuration for comparison of the effect of the parameters of interest.

Third, other studies have also pointed out the debonding effects (Immel et al. 2020) or bone damage at the interface (Ovesy et al. 2020) and their influence on micromotion and pull-out force. However, even if trabecular bone damage may occur during the insertion process, an experimental study showed that bone damage has no impact on the pull-out force (Bishop et al. 2014). As our study accounts for primary stability, this effect was neglected.

Fourth, a uniform thickness of cortical bone was considered. As the implant is only in contact with trabecular bone, it is assumed that the homogeneous thickness does not influence the results. A similar study on the ACI confirms this assumption with results showing that the influence of the cortical bone stiffness on the pull-out force is small compared to the other parameters (trabecular bone Young's modulus, friction coefficient and interference fit) (Immel et al. 2021).

Fifth, quasi-static analyses were carried out whereas the surgeons insert the implant by successive hammer impacts. In order to take into account viscoelastic effects of the bone, it would be interesting to consider dynamic simulations with implant impaction (Monea et al. 2014; Michel et al. 2017). Note that the computation cost required for such simulations would be considerably higher than the

one of the present study.

5 Conclusion

The present study brings new outcomes on the dependence of the vibration behavior of the bone-implant-ancillary system on the implant environment, which allow to open new path to monitor implant seating in terms of implant displacement and bone-implant contact. To the best of our knowledge, this is the first numerical study proposing modal analysis of the bone-implant-ancillary system at different FS insertion steps and with different biomechanical environments. Based on the results of this study, the vibration method could be used in patients with different bone qualities and for different surgical procedures defined by various values of friction coefficient and interference fit. The sensitivity of the resonance frequencies to the bone-implant contact ratio and to the bone quality may be used to develop a quantitative method to monitor FS insertion by means of vibration measurement on the ancillary, which is easily accessible during the surgical procedure. In addition, this study emphasizes the necessity to find a compromise on the interference fit and friction coefficient values, in order to maximize both the pull-out force and the *BIC* ratio. While the pull-out force is an increasing function of the interference fit, the trabecular bone Young's modulus and the friction coefficient, the *BIC* ratio is a decreasing one. Both the stability and the vibration features, that is, the pull-out forces and the resonance frequencies, respectively, are consistent with previous experimental results. However, the proposed *in silico* model should be improved in order to be more representative of the surgical impaction technique by simulating dynamic impacts.

6 Acknowledgments

The authors would like to thank Victor Housset for his feedback on the finite element model's geometry on the strength of its expertise as orthopedic surgeon.

7 Declarations

7.1 Ethic approval

Conflict of interest. The authors declare that they have no financial or non-financial interests that are directly or indirectly related to the work submitted for publication.

7.2 Authors' contribution

G.H, V.-H.N and G.R. conceived the study and were in charge of overall direction and planning. A.-S.P, and V.-H.N. designed the model and the computational framework. A.-S.P. performed the calculations. All authors participated to the analysis of the data. A-S.P. wrote the main manuscript text with inputs from all authors. All authors reviewed the manuscript.

7.3 Funding

This project has received funding from the European Research Council (ERC) under the European Union's Horizon 2020 research and innovation program (grant agreement No 682001, project ERC Consolidator Grant 2015 BoneImplant), from the project OrthAncil (ANR-21-CE19-0035-03) and from the project OrthoMat

(ANR-21-CE17-0004).

7.4 Availability of data and materials

The data that support the findings within this study are available from the corresponding author upon reasonable request.

References

M. P. Abdel, C. D. Watts, M. T. Houdek, D. G. Lewallen, and D. J. Berry. Epidemiology of periprosthetic fracture of the femur in 32 644 primary total hip arthroplasties: a 40-year experience. *The Bone & Joint Journal*, 98-B(4): 461–467, Apr. 2016. ISSN 2049-4408. doi: 10.1302/0301-620X.98B4.37201.

M. R. Abdul-Kadir, U. Hansen, R. Klabunde, D. Lucas, and A. Amis. Finite element modelling of primary hip stem stability: The effect of interference fit. *Journal of Biomechanics*, 41(3):587–594, Jan. 2008. ISSN 0021-9290. doi: 10.1016/j.jbiomech.2007.10.009.

L. E. Bayliss, D. Culliford, A. P. Monk, S. Glyn-Jones, D. Prieto-Alhambra, A. Judge, C. Cooper, A. J. Carr, N. K. Arden, D. J. Beard, and A. J. Price. The effect of patient age at intervention on risk of implant revision after total replacement of the hip or knee: a population-based cohort study. *The Lancet*, 389(10077):1424–1430, Apr. 2017. ISSN 0140-6736. doi: 10.1016/S0140-6736(17)30059-4.

H. H. Bayraktar, E. F. Morgan, G. L. Niebur, G. E. Morris, E. K. Wong, and T. M. Keaveny. Comparison of the elastic and yield properties of human femoral trabecular and cortical bone tissue. *Journal of Biomechanics*, 37(1):27–35, Jan. 2004. ISSN 0021-9290. doi: 10.1016/s0021-9290(03)00257-4.

N. E. Bishop, J.-C. Höhn, S. Rothstock, N. B. Damm, and M. M. Morlock. The influence of bone damage on press-fit mechanics. *Journal of Biomechanics*, 47 (6):1472–1478, Apr. 2014. ISSN 1873-2380. doi: 10.1016/j.jbiomech.2014.01.029.

N. E. Bishop, P. Wright, and M. Preutenborbeck. A parametric numerical analysis of femoral stem impaction. *Plos One*, 17(5), 2022. ISSN 1932-6203. doi: 10.1371/journal.pone.0268561.

R. Bosc, A. Tijou, G. Rosi, V.-H. Nguyen, J.-P. Meningaud, P. Hernigou, C.-H. Flouzat-Lachaniette, and G. Haiat. Influence of soft tissue in the assessment of the primary fixation of acetabular cup implants using impact analyses. *Clinical Biomechanics*, 55:7–13, June 2018. ISSN 02680033. doi: 10.1016/j.clinbiomech.2018.03.013.

T. D. Brown and A. B. Ferguson. Mechanical Property Distributions in the Cancellous Bone of the Human Proximal Femur. *Acta Orthopaedica Scandinavica*, 51(1-6):429–437, Jan. 1980. ISSN 0001-6470. doi: 10.3109/17453678008990819.

A. V. Carli, J. J. Negus, and F. S. Haddad. Periprosthetic femoral fractures and trying to avoid them: what is the contribution of femoral component design to the increased risk of periprosthetic femoral fracture? *The Bone & Joint Journal*, 99-B:50–59, Jan. 2017. ISSN 2049-4408. doi: 10.1302/0301-620X.99B1.BJJ-2016-0220.R1.

K. L. Corbett, E. Losina, A. A. Nti, J. J. Z. Prokopetz, and J. N. Katz. Population-based rates of revision of primary total hip arthroplasty: a systematic review. *Plos One*, 5(10), Oct. 2010. ISSN 1932-6203. doi: 10.1371/journal.pone.0013520.

N. B. Damm, M. M. Morlock, and N. E. Bishop. Friction coefficient and effective interference at the implant-bone interface. *Journal of Biomechanics*, 48(12):3517–3521, Sept. 2015. ISSN 1873-2380. doi: 10.1016/j.jbiomech.2015.07.012.

771 M. Dammak, A. Shirazi-Adl, M. Schwartz Jr., and L. Gustavson. Friction prop-
772 erties at the bone-metal interface: Comparison of four different porous metal
773 surfaces. *Journal of Biomedical Materials Research*, 35(3):329–336, 1997. ISSN
774 1097-4636. doi: 10.1002/(SICI)1097-4636(19970605)35:3⟨329::AID-JBM7⟩3.0.
775 CO;2-J.

776 A. S. Dickinson, A. C. Taylor, H. Ozturk, and M. Browne. Experimental validation
777 of a finite element model of the proximal femur using digital image correlation
778 and a composite bone model. *Journal of Biomechanical Engineering*, 133(1),
779 Jan. 2011. ISSN 1528-8951. doi: 10.1115/1.4003129.

780 C. Dopico-González, A. M. New, and M. Browne. Probabilistic finite element
781 analysis of the uncemented hip replacement–effect of femur characteristics and
782 implant design geometry. *Journal of Biomechanics*, 43(3):512–520, Feb. 2010.
783 ISSN 1873-2380. doi: 10.1016/j.jbiomech.2009.09.039.

784 R. Doyle, R. J. van Arkel, S. Muirhead-Allwood, and J. R. T. Jeffers. Impaction
785 technique influences implant stability in low-density bone model. *Bone & Joint*
786 *Research*, 9(7):386–393, July 2020. doi: 10.1302/2046-3758.97.BJR-2019-0303.
787 R1.

788 C. A. Engh, D. O'Connor, M. Jasty, T. F. McGovern, J. D. Bobyn, and W. H. Har-
789 ris. Quantification of implant micromotion, strain shielding, and bone resorption
790 with porous-coated anatomic medullary locking femoral prostheses. *Clinical Or-*
791 *thopaedics and Related Research*, (285):13–29, Dec. 1992. ISSN 0009-921X.

792 C. A. Engh, A. M. Young, C. A. Engh, and R. H. Hopper. Clinical consequences of
793 stress shielding after porous-coated total hip arthroplasty. *Clinical Orthopaedics*

and Related Research, (417):157–163, Dec. 2003. ISSN 0009-921X. doi: 10.1097/01.blo.0000096825.67494.e3.

R. H. J. Fitzgerald, G. W. Brindley, and B. F. Kavanagh. The Uncemented Total Hip Arthroplasty: Intraoperative Femoral Fractures. *Clinical Orthopaedics and Related Research*, 235:61–66, Oct. 1988. ISSN 0009-921X.

J. Folgado, P. Fernandes, C. Jacobs, and V. Pellegrini. Influence of femoral stem geometry, material and extent of porous coating on bone ingrowth and atrophy in cementless total hip arthroplasty: an iterative finite element model. *Computer Methods in Biomechanics and Biomedical Engineering*, 12(2):135–145, Apr. 2009. ISSN 1025-5842. doi: 10.1080/10255840802546754.

A. Gebert, J. Peters, N. E. Bishop, F. Westphal, and M. M. Morlock. Influence of press-fit parameters on the primary stability of uncemented femoral resurfacing implants. *Medical Engineering & Physics*, 31(1):160–164, Jan. 2009. ISSN 1350-4533. doi: 10.1016/j.medengphy.2008.04.007.

A. Herrera, J. J. Panisello, E. Ibarz, J. Cegoñino, J. A. Puértolas, and L. Gracia. Long-term study of bone remodelling after femoral stem: A comparison between dexa and finite element simulation. *Journal of Biomechanics*, 40(16):3615–3625, Jan. 2007. ISSN 0021-9290. doi: 10.1016/j.jbiomech.2007.06.008.

Y. Hériveaux, S. Le Cann, K. Immel, E. Vennat, V.-H. Nguyen, Brailovski, P. Karasinski, R. A. Sauer, and G. Haiat. Mechanical micromodeling of the bone-implant interphase under shear loading. *in press to Medical & Biological Engineering & Computing*, 2022.

K. Immel, T. X. Duong, V.-H. Nguyen, G. Haïat, and R. A. Sauer. A modified Coulomb's law for the tangential debonding of osseointegrated implants. *Biomechanics and Modeling in Mechanobiology*, 19(3):1091–1108, June 2020. ISSN 1617-7940. doi: 10.1007/s10237-019-01272-9.

K. Immel, V.-H. Nguyen, A. Dubory, C.-H. Flouzat–Lachaniette, R. A. Sauer, and G. Haïat. Determinants of the primary stability of cementless acetabular cup implants: A 3D finite element study. *Computers in Biology and Medicine*, 135: 104607, Aug. 2021. ISSN 00104825. doi: 10.1016/j.compbiomed.2021.104607.

M. G. Joshi, S. G. Advani, F. Miller, and M. H. Santare. Analysis of a femoral hip prosthesis designed to reduce stress shielding. *Journal of Biomechanics*, 33(12): 1655–1662, Dec. 2000. ISSN 0021-9290. doi: 10.1016/S0021-9290(00)00110-X.

F. Katsamanis and D. D. Raftopoulos. Determination of mechanical properties of human femoral cortical bone by the Hopkinson bar stress technique. *Journal of Biomechanics*, 23(11):1173–1184, Jan. 1990. ISSN 0021-9290. doi: 10.1016/0021-9290(90)90010-Z.

H. S. Khanuja, J. J. Vakil, M. S. Goddard, and M. A. Mont. Cementless Femoral Fixation in Total Hip Arthroplasty. *Journal of Bone and Joint Surgery*, 93(5): 500–509, Mar. 2011. ISSN 0021-9355, 1535-1386. doi: 10.2106/JBJS.J.00774.

Y. H. Kim, J. S. Kim, and S. H. Cho. Strain distribution in the proximal human femur. An in vitro comparison in the intact femur and after insertion of reference and experimental femoral stems. *The Journal of Bone and Joint Surgery. British Volume*, 83(2):295–301, Mar. 2001. ISSN 0301-620X. doi: 10.1302/0301-620x.83b2.10108.

T. Konow, J. Bätz, D. Beverland, T. Board, F. Lampe, K. Püschel, and M. M. Morlock. Variability in Femoral Preparation and Implantation Between Surgeons Using Manual and Powered Impaction in Total Hip Arthroplasty. *Arthroplasty Today*, 14:14–21, Apr. 2022. ISSN 2352-3441. doi: 10.1016/j.artd.2021.10.005.

J. H. Kuiper and R. Huiskes. The Predictive Value of Stress Shielding for Quantification of Adaptive Bone Resorption Around Hip Replacements. *Journal of Biomechanical Engineering*, 119(3):228–231, Aug. 1997. ISSN 0148-0731. doi: 10.1115/1.2796084.

J. N. Lamb, G. S. Matharu, A. Redmond, A. Judge, R. M. West, and H. G. Pandit. Risk Factors for Intraoperative Periprosthetic Femoral Fractures During Primary Total Hip Arthroplasty. An Analysis From the National Joint Registry for England and Wales and the Isle of Man. *The Journal of Arthroplasty*, 34 (12):3065–3073, Dec. 2019. ISSN 1532-8406. doi: 10.1016/j.arth.2019.06.062.

S. Leuridan, Q. Goossens, L. Pastrav, J. Roosen, M. Mulier, K. Denis, W. Desmet, and J. V. Sloten. Determination of replicate composite bone material properties using modal analysis. *Journal of the Mechanical Behavior of Biomedical Materials*, 66:12–18, 2017. ISSN 1878-0180. doi: 10.1016/j.jmbbm.2016.10.018.

S. Leuridan, Q. Goossens, L. C. Pastrav, M. Mulier, W. Desmet, J. Vander Sloten, and K. Denis. Development of an Instrument to Assess the Stability of Cementless Femoral Implants Using Vibration Analysis During Total Hip Arthroplasty. *IEEE Journal of Translational Engineering in Health and Medicine*, 9: 1–10, 2021. ISSN 2168-2372. doi: 10.1109/JTEHM.2021.3128276.

C. K. McCarthy, G. G. Steinberg, M. Agren, D. Leahey, E. Wyman, and D. T.

Baran. Quantifying bone loss from the proximal femur after total hip arthroplasty. *The Journal of Bone and Joint Surgery. British Volume*, 73(5):774–778, Sept. 1991. ISSN 0301-620X. doi: 10.1302/0301-620X.73B5.1894664.

A. Michel, V.-H. Nguyen, R. Bosc, R. Vayron, P. Hernigou, S. Naili, and G. Haiat. Finite element model of the impaction of a press-fitted acetabular cup. *Medical & Biological Engineering & Computing*, 55(5):781–791, May 2017. ISSN 0140-0118, 1741-0444. doi: 10.1007/s11517-016-1545-2.

A. G. Monea, L. C. Pastrav, M. Mulier, G. Van der Perre, and S. V. Jaecques. Numerical simulation of the insertion process of an uncemented hip prosthesis in order to evaluate the influence of residual stress and contact distribution on the stem initial stability. *Computer Methods in Biomechanics and Biomedical Engineering*, 17(3):263–276, 2014. ISSN 1476-8259. doi: 10.1080/10255842.2012.681644.

M. Mulier, C. Pastrav, and G. Van der Perre. Per-operative vibration analysis: a valuable tool for defining correct stem insertion: preliminary report. *Ortopedia, Traumatologia, Rehabilitacja*, 10(6):576–582, Dec. 2008. ISSN 1509-3492.

V.-H. Nguyen, G. Rosi, S. Naili, A. Michel, M.-L. Raffa, R. Bosc, J.-P. Meningaud, C. Chappard, N. Takano, and G. Haiat. Influence of anisotropic bone properties on the biomechanical behavior of the acetabular cup implant: a multi-scale finite element study. *Computer Methods in Biomechanics and Biomedical Engineering*, 20(12):1312–1325, Sept. 2017. ISSN 1025-5842, 1476-8259. doi: 10.1080/10255842.2017.1357703.

M. Ovesy, B. Voumard, and P. Zysset. A nonlinear homogenized finite element

analysis of the primary stability of the bone-implant interface. *Biomechanics and Modeling in Mechanobiology*, 17(5):1471–1480, Oct. 2018. ISSN 1617-7940. doi: 10.1007/s10237-018-1038-3.

M. Ovesy, M. Aeschlimann, and P. K. Zysset. Explicit finite element analysis can predict the mechanical response of conical implant press-fit in homogenized trabecular bone. *Journal of Biomechanics*, 107:109844, June 2020. ISSN 1873-2380. doi: 10.1016/j.jbiomech.2020.109844.

L. C. Pastrav, J. Devos, G. Van der Perre, and S. V. N. Jaecques. A finite element analysis of the vibrational behaviour of the intra-operatively manufactured prosthesis-femur system. *Medical Engineering & Physics*, 31(4):489–494, May 2009a. ISSN 1873-4030. doi: 10.1016/j.medengphy.2008.11.017.

L. C. Pastrav, S. V. Jaecques, I. Jonkers, G. V. d. Perre, and M. Mulier. In vivo evaluation of a vibration analysis technique for the per-operative monitoring of the fixation of hip prostheses. *Journal of Orthopaedic Surgery and Research*, 4: 10, Apr. 2009b. ISSN 1749-799X. doi: 10.1186/1749-799X-4-10.

S. H. Pettersen, T. S. Wik, and B. Skallerud. Subject specific finite element analysis of implant stability for a cementless femoral stem. *Clinical Biomechanics*, 24(6): 480–487, July 2009. ISSN 0268-0033. doi: 10.1016/j.clinbiomech.2009.03.009.

R. Pivec, A. J. Johnson, S. C. Mears, and M. A. Mont. Hip arthroplasty. *The Lancet*, 380(9855):1768–1777, Nov. 2012. ISSN 1474-547X. doi: 10.1016/S0140-6736(12)60607-2.

A.-S. Poudrel, G. Rosi, V.-H. Nguyen, and G. Haiat. Modal Analysis of the Ancillary During Femoral Stem Insertion: A Study on Bone Mimicking Phantoms.

Annals of Biomedical Engineering, 50(1):16–28, Jan. 2022. ISSN 1573-9686. doi: 10.1007/s10439-021-02887-9.

M. A. Pérez and B. Seral-García. A finite element analysis of the vibration behaviour of a cementless hip system. *Computer Methods in Biomechanics and Biomedical Engineering*, 16(9):1022–1031, 2013. ISSN 1476-8259. doi: 10.1080/10255842.2011.650635.

M. L. Raffa, V.-H. Nguyen, and G. Haiat. Micromechanical modeling of the contact stiffness of an osseointegrated bone–implant interface. *BioMedical Engineering OnLine*, 18(1):114, Dec. 2019a. doi: 10.1186/s12938-019-0733-3.

M. L. Raffa, V.-H. Nguyen, E. Tabor, K. Immel, V. Housset, C.-H. Flouzat-Lachaniette, and G. Haiat. Dependence of the primary stability of cementless acetabular cup implants on the biomechanical environment. *Proceedings of the Institution of Mechanical Engineers. Part H, Journal of Engineering in Medicine*, 233(12):1237–1249, Dec. 2019b. ISSN 2041-3033. doi: 10.1177/0954411919879250.

M. L. Raffa, V.-H. Nguyen, P. Hernigou, C.-H. Flouzat-Lachaniette, and G. Haiat. Stress shielding at the bone-implant interface: Influence of surface roughness and of the bone-implant contact ratio. *Journal of Orthopaedic Research: Official Publication of the Orthopaedic Research Society*, 39(6):1174–1183, June 2021. doi: 10.1002/jor.24840.

M. Reimeringer and N. Nuño. The influence of contact ratio and its location on the primary stability of cementless total hip arthroplasty: A finite element analysis.

Journal of Biomechanics, 49(7):1064–1070, May 2016. ISSN 0021-9290. doi: 10.1016/j.jbiomech.2016.02.031.

M. Reimeringer, N. Nuño, C. Desmarais-Trépanier, M. Lavigne, and P. A. Vendittoli. The influence of uncemented femoral stem length and design on its primary stability: a finite element analysis. *Computer Methods in Biomechanics and Biomedical Engineering*, 16(11):1221–1231, 2013. ISSN 1476-8259. doi: 10.1080/10255842.2012.662677.

S. Rothstock, A. Uhlenbrock, N. Bishop, and M. Morlock. Primary stability of uncemented femoral resurfacing implants for varying interface parameters and material formulations during walking and stair climbing. *Journal of Biomechanics*, 43(3):521–526, Feb. 2010. ISSN 0021-9290. doi: 10.1016/j.jbiomech.2009.09.052.

R. D. Russell, M. H. Huo, D. C. Rodrigues, and V. Kosmopoulos. Stem geometry changes initial femoral fixation stability of a revised press-fit hip prosthesis: A finite element study. *Technology and Health Care: Official Journal of the European Society for Engineering and Medicine*, 24(6):865–872, Nov. 2016. ISSN 1878-7401. doi: 10.3233/THC-161235.

A. Shirazi-Adl, M. Dammak, and G. Paiement. Experimental determination of friction characteristics at the trabecular bone/porous-coated metal interface in cementless implants. *Journal of Biomedical Materials Research*, 27(2):167–175, Feb. 1993. ISSN 0021-9304. doi: 10.1002/jbm.820270205.

T. R. Shultz, J. D. Blaha, T. A. Gruen, and T. L. Norman. Cortical bone viscoelasticity and fixation strength of press-fit femoral stems: finite element model.

952 *Journal of Biomechanical Engineering*, 128(1):7–12, Feb. 2006. ISSN 0148-0731.
953 doi: 10.1115/1.2133765.

954 C. C. Sidler-Maier and J. P. Waddell. Incidence and predisposing factors of
955 periprosthetic proximal femoral fractures: a literature review. *International*
956 *Orthopaedics*, 39(9):1673–1682, Sept. 2015. ISSN 1432-5195. doi: 10.1007/
957 s00264-015-2721-y.

958 M. Sloan, A. Premkumar, and N. P. Sheth. Projected Volume of Primary Total
959 Joint Arthroplasty in the U.S., 2014 to 2030. *The Journal of Bone and Joint*
960 *Surgery. American Volume*, 100(17):1455–1460, Sept. 2018. ISSN 1535-1386.
961 doi: 10.2106/JBJS.17.01617.

962 M. Taylor, K. E. Tanner, M. A. Freeman, and A. L. Yettram. Cancellous bone
963 stresses surrounding the femoral component of a hip prosthesis: an elastic-plastic
964 finite element analysis. *Medical Engineering & Physics*, 17(7):544–550, Oct.
965 1995. ISSN 1350-4533. doi: 10.1016/1350-4533(95)00018-i.

966 A. Tijou, G. Rosi, R. Vayron, H. A. Lomami, P. Hernigou, C.-H. Flouzat-
967 Lachaniette, and G. Haïat. Monitoring cementless femoral stem insertion
968 by impact analyses: An in vitro study. *Journal of the Mechanical Behav-*
969 *ior of Biomedical Materials*, 88:102–108, Dec. 2018. ISSN 17516161. doi:
970 10.1016/j.jmbbm.2018.08.009.

971 S. D. Ulrich, T. M. Seyler, D. Bennett, R. E. Delanois, K. J. Saleh, I. Thong-
972 trangan, M. Kuskowski, E. Y. Cheng, P. F. Sharkey, J. Parvizi, J. B. Stiehl,
973 and M. A. Mont. Total hip arthroplasties: What are the reasons for revision?

974 *International Orthopaedics*, 32(5):597–604, Oct. 2008. ISSN 0341-2695. doi:
975 10.1007/s00264-007-0364-3.

976 uncemented femoral stem. CERAFIT RMIS HAC, Ceraver, Sept. 2020. URL
977 https://www.ceraver.com/cerafit-rmis-hac/.

978 A. S. Wong, A. M. R. New, G. Isaacs, and M. Taylor. Effect of bone material
979 properties on the initial stability of a cementless hip stem: a finite element
980 study. *Proceedings of the Institution of Mechanical Engineers. Part H, Journal*
981 *of Engineering in Medicine*, 219(4):265–275, July 2005. ISSN 0954-4119. doi:
982 10.1243/095441105X34293.

983 P. Wriggers. *Computational Contact Mechanics*. Springer, 2006.